Published in final edited form as:
Annu Rev Phys Chem. 2011 ; 62: 507–530. doi:10.1146/annurev.physchem.012809.103512.

Coherent Nonlinear Optical Imaging: Beyond Fluorescence Microscopy

Wei Min[1,*], **Christian W. Freudiger**[1,2], **Sijia Lu**[1], and **X. Sunney Xie**[1,†]

[1]Department of Chemistry and Chemical Biology, Harvard University, Cambridge 02138, MA

[2]Department of Physics, Harvard University, Cambridge 02138, MA

Abstract

The quest for ultrahigh detection sensitivity with spectroscopic contrasts other than fluorescence has led to various novel approaches to optical microscopy of biological systems. Coherent nonlinear optical imaging, especially the recently developed nonlinear dissipation microscopy, including stimulated Raman scattering and two photon absorption, and pump-probe microscopy, including stimulated emission, excited state absorption and ground state depletion, provide distinct and powerful image contrasts for non-fluorescent species. Thanks to high-frequency modulation transfer scheme, they exhibit superb detection sensitivity. By directly interrogating vibrational and/or electronic energy levels of molecules, they offer high molecular specificity. Here we review the underlying principles, excitation and detection schemes, as well as exemplary biomedical applications of this emerging class of molecular imaging techniques.

INTRODUCTION

Modern optical microscopy is intimately related to molecular spectroscopy. Fundamentally speaking, various optically induced molecular spectroscopic transitions, linear or nonlinear, coherent or incoherent, can all be used to provide distinct imaging contrast mechanisms for optical microscopy. As the underlying molecular spectroscopic and imaging scheme vary, the corresponding microscopy will exhibit different levels of detection sensitivity and provide contrast information with different degrees of molecular selectivity.

Fluorescence spectroscopy (1) and microscopy (2), combined with the ever-expanding palette of genetically encoded fluorescent proteins (3-5) or exogenous dyes or semiconductor nanocrystals (6), is currently the most popular imaging contrast used in biological studies. This is mainly because of the exquisite specificity given by the art of targeted probe labeling and the unprecedented sensitivity offered by the intense electronic transition dipole moment and background-free fluorescence detection. As such, various versatile fluorescence-based techniques have flourished such as confocal laser scanning (2), two-photon excited fluorescence (7), single-molecule microscopy (8, 9) and super-resolution imaging (10).

However, many molecular species are intrinsically non-fluorescent or only weakly fluorescent. In addition, fluorescent labels, natural or artificial, are often perturbative, especially for small molecules such as signaling peptides, metabolites, neurotransmitters and

†xie@chemistry.harvard.edu.
*Current address: Department of Chemistry, Columbia University, New York, NY 10027

DISCLOSURE STATEMENT
Patents and patent applications held by Harvard University have been licensed to multiple microscope manufacturers.

drugs, whose sizes are even smaller than the fluorescent labels. Moreover, it is better not to use labeling or staining with fluorophores *in vivo* medical applications on humans. Hence, optical imaging methods with high sensitivity and specific molecular contrasts other than fluorescence are highly desirable in biomedical and material science.

Unlike fluorescence which is an incoherent process, coherent nonlinear molecular spectroscopy can generate a plethora of optical signals that do not rely on fluorescence emission. Thus, they are extremely useful tools offering contrast mechanisms for label-free chemical imaging. Depending on the underlying nonlinear optical processes, they can be grouped into the following three distinct categories:

1. parametric generation spectroscopy in which incident and outgoing laser fields exchange energy with each other while molecules remain in the ground state after interaction, including second harmonic generation, third harmonic generation, four-wave-mixing process, and coherent anti-Stokes Raman scattering (CARS);
2. nonlinear dissipation optical spectroscopy in which molecules exchange energy with incident laser fields (normally at two different wavelengths, pump and probe, respectively) after interaction, including stimulated Raman scattering and two-photon absorption;
3. pump-probe spectroscopy in which the pump pulse is used to excite molecules and the subsequent probe pulse to interrogate the transient states through stimulated emission, excited state absorption, or ground state depletion. In contrast to the above two categories, a certain time delay between the pump and probe pulses is often necessary to allow for dynamic evolution of the molecular states.

While the parametric generation spectroscopy has been extensively studied and utilized for optical microscopy, the demonstration and application of nonlinear dissipation spectroscopy and pump-probe spectroscopy for chemical imaging have only been recently explored. Experimentally, nonlinear dissipation microscopy and pump-probe microscopy all use femtosecond or picosecond mode-locked pulse trains, which have high peak power but low average power, and can employ a similar high-frequency modulation transfer scheme to achieve high sensitivity (11). In addition, these two categories carry specific spectroscopic signatures by directly interrogating vibrational resonance and/or electronic resonance energy levels of molecules.

A generic modulation transfer scheme for nonlinear dissipation microscopy and pump-probe microscopy is depicted in Fig.1. First, two temporally synchronized ultrafast laser pulse trains (pump and probe) are spatially combined and focused collinearly onto a common focal spot in the sample. Second, before the sample, the intensity (in principle other quantities such as frequency, phase and polarization as well) of the pump beam is modulated at a high frequency f (>1 MHz), while the probe beam is originally un-modulated. After interacting with the sample at the common focal volume, only the intensity of the probe beam is collected and detected by a photodiode. The readout of the photodiode is then demodulated by a lock-in amplifier to extract the modulation depth at the frequency f. Third, with the amount of the modulation transfer being registered for each pixel, a three-dimensional (3D) image is then constructed by scanning the combined pump/probe laser beams across the sample point-by-point with a laser scanning microscope.

The high frequency of f is crucial for achieving desirable imaging sensitivity. Laser intensity noise occurs primarily at low frequencies (from kHz to DC) in the form of the so-called $1/f$ noise, as shown in Fig.1(c). As f goes above the MHz range, the laser intensity noise gradually approaches the floor of quantum shot noise which is always present due to the stochastic arrivals of photons at the detector. Therefore, the narrow-band modulation/

demodulation at f removes the low-frequency $1/f$ laser intensity noise and allows for shot-noise limited detection sensitivity. Moreover, as the focused laser beam is scanned across the specimen, the intensity variation due to scattering from heterogeneous biological samples will be filtered out by the high-frequency lock-in amplifier because those intensity variations occur at relatively slow scanning frequencies.

The same quantitative feature is shared among these modulation transfer techniques. Under the unsaturated condition, the signal strength, S, which is defined as the amount of intensity modulation generated to the originally unmodulated probe beam at the frequency f, is proportional to the product of the pump beam intensity, I_{pump}, the probe beam intensity, I_{probe}, the analyte concentration, $[c]$, and a specific molecular cross section of the analyte, $\sigma_{molecule}$, for the corresponding optical process:

$$S \propto [c] \cdot \sigma_{\text{molecule}} \cdot I_{pump} \cdot I_{probe} \quad [1]$$

Because of the overall quadratic intensity dependence, the signal is only generated at the laser focus where the optical intensity is the highest. Such a nonlinearity allows for 3D optical sectioning without the use of a confocal pinhole, similar to two-photon excited fluorescence microscopy (7). This is also the reason why these techniques are considered as nonlinear optical microscopy. In addition, the linear concentration dependence of the analyte permits straightforward quantification, as opposed to the parametric generation microscopy which often exhibits quadratic concentration dependence. Table 1 summazies their important physical properties and the resulting desirable consequence in bio-imaging practice.

PARAMETRIC GENERATION MICROSCOPY

In all the parametric generation processes, a coherent radiation is generated at a color different from those of the incident laser beams, making its spectral separation and detection convenient. Hence, this is the category that has received the most extensive studies. Among them, second harmonic generation (12-14), third harmonic generation (15, 16) and four-wave-mixing (17-19) microscopy all utilize nonlinear electronic polarization of the molecules under laser pulse excitation. In particular, second harmonic generation, being sensitive to molecular symmetry breaking, has found useful applications in a number of biological systems such as imaging collagen distribution (20, 21) and membrane potential (14). However, because no real vibrational or electronic quantum states of the molecules are directly probed, the information about the internal molecular identity in these contrast mechanisms is limited.

Another member of the nonlinear parametric generation processes is CARS (22) which probes vibrational states of molecules and is intimately related to spontaneous Raman scattering. Due to the fact that spontaneous Raman cross sections are typically 10~12 orders of magnitudes smaller than the absorption cross section, spontaneous Raman microscopy often requires very long acquisition time (23). In addition, the unavoidable auto-fluorescence background of biological specimen often overwhelms the feeble spontaneous Raman signal from the target chemical species. As a third-order nonlinear Raman process, however, CARS is capable of circumventing the feebleness of spontaneous Raman scattering by driving and detecting the vibrational coherence of an ensemble of molecules within the laser focus (11, 22, 24, 25). In brief, when the energy difference, Ω, between the pump and probe (also called Stokes beam in the Raman literature) matches the energy gap, ω_v, of a particular vibrational transition, $\Omega \equiv \omega_{pump} - \omega_{probe} \rightarrow \omega_v$, then the (difference frequency) beating between the pump and probe beams will drive the vibrational oscillators within the focus coherently in phase. As shown in Fig. 2(a), the resulting vibrational

coherence (i.e. ρ_{vib}., the off-diagonal element of the density matrix characterizing the degree to which the molecules in the ensemble oscillate in unison) is further read out by additional scattering off the pump beam to generate a coherent radiation at the anti-Stokes frequency $\omega_{as} = 2\omega_{pump} - \omega_{probe}$.

Quantitatively, the ratio between resonant CARS and spontaneous Raman emission radiation rates is approximately proportional to the number of vibrational oscillators, N, in the excitation volume and the square of the coherence amplitude ρ_{vib}.: $r_{CARS}/r_{spon.Raman} \approx N \cdot |\rho_{vib}|$. (26, 27). A crude estimate of the coherence follows $\rho_{vib}. \approx \Xi_{pump} \cdot \Xi_{probe} \cdot \tau/\Delta$, where $\Xi_{pump,\ probe}$ is the Rabi frequency of pump or probe field, respectively, τ is the pulse length, and Δ is the detuning from the electronic resonance. While the intensity of incoherent emission of spontaneous Raman is simply proportional to the number of incoherent emitters, the CARS fields produced by coherent emitters add up in amplitude first and are then squared to produce intensity. Hence CARS intensity grows as the number of coherent emitters squared, which has been demonstrated in microscopy configuration experimentally (28). Therefore, it is the constructive interference among all the coherent vibrational oscillators within the focus that gives rise to amplification of the coherent radiation.

However, the CARS signal does not completely vanish even when Ω is tuned off from all the vibrational resonance, as many theoretical and experimental studies have verified. Such a “non-resonant background” is actually a four-wave-mixing parametric generation process (11, 24, 25), as shown in Fig. 2(b), and is generated by the nonlinear electronic response of the sample mediated through virtual states. This background poses serious problems for CARS microscopy in two interrelated ways (29-31). First, as described by the last term of the following equation,

$$I_{CARS}(\Omega) \propto \left(\left|\chi_R^{(3)}(\Omega)\right|^2 + \left|\chi_{NR}^{(3)}\right|^2 + 2\chi_{NR}^{(3)}\mathrm{Re}\left[\chi_R^{(3)}(\Omega)\right]\right) \cdot {I_{pump}}^2 \cdot I_{probe} \qquad [2]$$

the non-resonant background electric field distorts the CARS spectrum due to its constructive and destructive interference with the resonant vibrational contribution, $\mathrm{Re}\left[\chi_R^{(3)}(\Omega)\right]$, on the red and blue sides of the Raman peak, respectively (22). Such a spectral distortion effect results in a CARS spectrum that differs from the corresponding spontaneous Raman spectrum (as illustrated by Fig. 3(a) and (b)), which is even more complicated in the congested fingerprint region. Second, it limits the detection sensitivity of CARS microscopy. In the scenario of dilute analytes, $\left|\chi_R^{(3)}(\Omega)\right|^2 \ll \left|\chi_{NR}^{(3)}\right|^2$ and Eq. (2) simplifies to $I_{CARS}(\Omega) \propto \left|\chi_{NR}^{(3)}\right|^2 + 2\chi_{NR}^{(3)}\mathrm{Re}\left[\chi_R^{(3)}(\Omega)\right]$. The signal-to-noise ratio of CARS detection then becomes

$$SNR_{CARS} \propto \frac{2\chi_{NR}^{(3)}\mathrm{Re}\left[\chi_R^{(3)}(\Omega)\right] \cdot {I_{pump}}^2 \cdot I_{probe}}{\alpha \cdot \left|\chi_{NR}^{(3)}\right| \cdot {I_{pump}}^2 \cdot I_{probe} + \chi_{NR}^{(3)} \cdot {I_{pump}}^2 \cdot I_{probe} + \chi_{NR}^{(3)} \cdot I_{pump} \cdot \sqrt{I_{probe}}} \overset{\alpha \to 0}{\Rightarrow} 2\mathrm{Re}\left[\chi_R^{(3)}(\Omega)\right] \cdot I_{pump} \cdot \sqrt{I_{probe}}$$

where $\alpha \cdot \left|\chi_{NR}^{(3)}\right|^2 \cdot {I_{pump}}^2 \cdot I_{probe}$ denotes the low-frequency intensity noise carried by the non-resonant background due to the $1/f$ noise of the excitation lasers, and $\chi_{NR}^{(3)} \cdot I_{pump} \cdot \sqrt{I_{probe}}$ is the shot noise of the non-resonant background. The shot noise limit is reached only in the ideal situation in which α is vanishing, $SNR_{CARS} \to 2\mathrm{Re}\left[\chi_R^{(3)}(\Omega)\right] \cdot I_{pump} \cdot \sqrt{I_{probe}}$..

The first CARS microscope was reported in 1982 (32). The noncollinear geometry used did not allow 3D imaging and the visible dye laser employed generated large nonresonant background via two photon electronic resonance, which overwhelmed the vibrationally

resonant signals. Because of these difficulties, the technique was not adopted for a long time. In 1999, three dimensional CARS imaging of living cells was achieved (33) by tightly focusing collinear pump and Stokes beams, which allowed 3D sectioning, and a near-infrared laser system was employed to suppresse the non-resonant background. This work triggered rapid developments and widespread activities.

Being a parametric generation processes, CARS needs to satisfy the phase matching condition, which is a consequence of the conservation of momentum. In conventional spectroscopy experiments as well the early microscopy work (32, 33), the CARS signal was detected in the phase matching direction. Under the tightly focusing condition for microscopy, however, the large cone angle of the k vectors of the pump and Stokes beams relax the phase matching condition. As a result, the CARS signal generated has a large cone angle of the k vector as well, even in the backward direction for an object with a size comparable to or smaller than the CARS wavelength, or for an interface between two media with different $\chi^{(3)}$ (29, 34). This results from the constructive and destructive interference of CARS radiation from different parts of the sample. Hence the CARS image has a complicated dependence on the exact object geometry. Image deconvolution with a point spread function, as is often employed in fluorescence microscopy, is no longer possible. An example of this is shown in Fig. 3(g) for individual polymer bead that exhibits a donut shape image in the backward direction. The forward and backward images are not the same. Complication by such a spatial coherence effect makes the interpretation of CARS images difficult unless prior knowledge of the object's exact geometry is available.

We note that another mechanism for CARS signal detected in the backward direction is the forward going CARS being reflected backward by scattering after focal plane, which explains the observed dot at the center of each bead in Fig 3(g). The backward reflected CARS in highly scattering tissue samples is strong enough to allow recording CARS movies on living animals with video rate (35). A major application of CARS microscopy in biomedicine has been in imaging structure and dynamics of lipids which have abundant C-H stretching oscillators with a spectrally isolated Raman band. Applications have been reported at various levels including cellular (36), tissue (37, 38) and organism (39, 40).

In the past decade, numerous methods have been developed to suppress or circumvent the non-resonant background, including epi detection (29, 34), polarization CARS (41, 42), time-resolved CARS (43), interferometric or heterodyne CARS (44-49), femtosecond pulse shaping (50-53), phase retrieval CARS (54, 55), and frequency modulation CARS (56, 57). These methods have demonstrated varying degrees of success in removal of the non-resonant background and simplification of image interpretation. However, most of them were hampered by increased complexity of instrumentation and data analysis. With the exception of interferometric CARS, all of these methods still cannot resolve the complication due to phase matching and spatial coherence. Moreover, in spatially heterogeneous biological samples, phase or polarization sensitive imaging methods are ultimately limited in sensitivity because of variations of the refractive index and birefringence.

NONLINEAR DISSIPATION MICROSCOPY

The phenomenon of stimulated Raman scattering (SRS) was discovered immediately after the laser was invented (58-60). When a cell filled with nitrobenzene was introduced into a ruby laser cavity, Woodbury and Ng observed a rather strong emission at a new wavelength other than the fundamental wavelength of ruby laser, which was later understood as stimulated Raman gain (58). Two years later, a related phenomenon, stimulated Raman loss (or inverse Raman) was also discovered (59). Since then stimulated Raman spectroscopy has

been performed on various physical and chemical systems (61-63). In particular, femtosecond stimulated Raman spectroscopy has been developed to provide vibrational structural information with both high temporal and spectral information of chromophore systems such as primary photoisomerization and green fluorescent protein (64, 65).

SRS probes the excited vibrational population instead of the vibrational coherence detected by CARS (11, 25, 60). When Ω is tuned into a vibrational resonance, $\Omega \rightarrow \omega_v$, due to the combined interaction of the incident pump and probe beams, the rate of the vibrational excitation will be greatly accelerated compared to that in spontaneous Raman scattering by a factor given by

$$\frac{r_{\text{stim.Raman}}}{r_{\text{spon.Raman}}} = n_{probe} + 1 \tag{4}$$

where n_{probe} is the (normally large) number of photons in the optical mode of the probe beam (25). Such efficient excitation of a molecular vibrational level obviously requires energy input from the laser fields. As required by energy conservation, for each quantum of the vibrational excitation being excited, it is accompanied by one photon being annihilated from the pump beam and simultaneously a photon being created into the probe beam (Fig. 4 (a)). The resulting intensity loss in the pump beam is called stimulated Raman loss, and the intensity gain in the probe beam is called stimulated Raman gain.

Stimulated Raman gain and loss can also be understood in the semi-classical framework of nonlinear induced polarization (60) as an optical heterodyne phenomenon. When $\Omega \rightarrow \omega_v$, besides the CARS radiation at the anti-Stokes frequency, two other third-order induced polarizations, p_{pump} and p_{probe}, are generated at the fundamental pump and probe frequencies, shown in Fig. 2(c) and (d), respectively: $p_{pump} \propto \chi_R^{(3)}(\Omega) \cdot E_{pump} \cdot E_{probe}^2$ and $p_{probe} \propto \chi_R^{(3)}(\Omega) \cdot E_{probe} \cdot E_{pump}^2 \cdot p_{pump}$ and p_{probe} propagate in the forward direction and interfere with the incident pump and probes fields with their corresponding phases. For stimulated Raman gain, p_{probe} constructively interferes with E_{probe} and results in an intensity gain:

$$Gain_{probe} = 2 \cdot p_{probe} \cdot E_{probe} \propto 2\text{Im}\left|\chi_R^{(3)}(\Omega)\right| \cdot I_{probe} \cdot I_{pump} \tag{5a}$$

For stimulated Raman loss, p_{pump} destructively interferes with E_{pump} and results in an intensity loss:

$$LOSS_{pump} = -2 \cdot p_{pump} \cdot E_{pump} \propto -2\text{Im}\left[\chi_R^{(3)}(\Omega)\right] \cdot I_{probe} \cdot I_{pump} \tag{5b}$$

Such an optical heterodyne interpretation is analogous to the picture that linear absorption can be treated as the destructive interference between the incident field and linear induced polarization of the molecule at the forward detector.

SRS as a contrast mechanism for microscopy was first reported using multiplex detection with a photodiode array in combination with a femtosecond amplified laser system (66). Although the amplified laser system generates a large SRS signal, it is not suitable for bio-imaging because the excessive peak power causes sample damage and the low repetition rate limits the image acquisition speed. Instead, using narrow-band picosecond pulse trains with high repetition rates, stimulated Raman scattering was later adapted into a high-frequency modulation transfer microscopy by several groups (67-69). Very recently, its multiplex version has been developed into a spectral imaging modality by using a spectrally shaped broadband excitation pulse (70). When the pump beam is blocked, the probe beam maintains

its intensity after passing through the sample; when the pump beam is unblocked, the probe beam experiences stimulated Raman gain due to nonlinear interactions. Hence, a temporal modulation of the pump beam intensity at a frequency *f* would give rise to a modulation of the probe beam intensity, at the same frequency *f*, after interacting with the vibrational oscillators at the foci.

SRS imaging is free from the non-resonant background in CARS microscopy. Fig. 3(f) shows the simultaneous SRS CH_2 image of the same worm sample in Fig. 3(e). Only purely lipid contrast is visible in SRS. This is so because, in the absence of a vibrational eigenstate that could hold the population and energy, energy simply cannot transfer from the pump beam to the probe beam, as required by energy conservation. In the optical heterodyne picture, the off-resonant polarization fields are either 90 degree ahead or 90 degree behind the incident pump or probe fields at the detector, which forbids any constructive or destructive interference (and hence intensity gain or loss) with the pump or probe beams from occurring.

Such a drastic contrast between SRS and CARS is analogous to the more familiar relation between absorption and Rayleigh scattering. While linear absorption by a molecule can be tuned off completely from its absorption band, Rayleigh scattering always occurs even if there is no resonance between the light and the molecule. Physically, scattering events can be mediated by a virtual state, while absorption events cannot. To some extent, SRS and CARS can be viewed as the nonlinear Raman analog of the linear absorption and Rayleigh scattering phenomena, respectively.

SRS overcomes all major difficulties associated with CARS microscopy, as summarized in Table 2. First, the absence of the non-resonant background eliminates the biggest obstacle for CARS imaging quantification and interpretation. Second, without the interference effect from the background, the SRS spectrum is identical to that of spontaneous Raman scattering (Fig. 4b), allowing the straightforward utilization of all the accumulated knowledge of Raman spectroscopy. Third, the detection sensitivity of SRS is demonstrated to be much higher than that of CARS microscopy. The signal-to-noise ratio of SRS detection may be written

$$SNR_{SRS} = \frac{2\mathrm{Im}\left[\chi_R^{(3)}(\Omega)\right] \cdot I_{\mathrm{pump}} \cdot I_{probe}}{\alpha \cdot I_{probe} + \sqrt{I_{probe}}} \overset{\alpha \to 0}{\Rightarrow} 2\mathrm{Im}\left[\chi_R^{(3)}(\Omega)\right] \cdot I_{pump} \cdot \sqrt{I_{probe}} \qquad (6)$$

where $\alpha \cdot I_{probe}$ denotes the laser intensity noise of the probe beam, and $\sqrt{I_{probe}}$ is the shot noise of the probe beam intensity. Thanks to the high-frequency modulation and lock-in detection at a high *f*, $\alpha \cdot I_{probe}$ can be readily removed in SRS detection. With $\alpha \to 0$, SRS can reach the shot noise limit, with detectable $\Delta I_p / I_p$ approaching 10^{-8} within one second of acquisition time.

It is worth noting that, based on Eqs. (3) and (6), $SNR_{CARS}\big|_{\alpha \to 0} \approx SNR_{\mathrm{SRS}}\big|_{\alpha \to 0}$ in the scenario in which laser intensity fluctuation can be completely eliminated and the shot noise (from non-resonant background and the probe beam for CARS and SRS, respectively) is the only remaining noise source. However, it is extremely hard for CARS to meet this ideal situation, because of the difficulty of employing an effective high frequency modulation technique. In CARS, when certain optical properties (e.g., frequency) of the pump or probe beam are modulated, the non-resonant background almost always leaves spurious intensity noise. In contrast, the probe beam in SRS is unperturbed before interacting with the sample, and its intensity noise can be circumvented with ease by modulation transfer.

Moreover, SRS exhibits a few other favorable properties over CARS (Table 2). The concentration dependence of CARS turns over from a quadratic in high concentration limit to a linear in the limit of low analyte concentration (Eq. (2)), with the exact quantitative relation depending on the nonlinear nature of the surrounding solvent. In contrast, the strict linear concentration dependence of SRS permits straightforward and reliable quantification. In addition, because SRS involves measurements of transmission differences of the input beams, SRS is automatically phase matched. Hence, there exists a well-defined point spread function that can be used for image deconvolution (Fig. 3(h)). Therefore, the image contrast in SRS microscopy is easy to understand, because it is free from spatial coherence artifacts.

Although the phase matching condition dictates that the SRS effect be detected by measuring the transmitted pump or Stoke beams in the forward direction, it is desirable to detect SRS in the backward direction for thick, non-transparent tissue samples as light does not penetrate through them. Fortunately, this can be done if a large area detector is used to collect a significant portion of the back-scattered light after the SRS signal is already generated at the laser focus (71).

Compared to spontaneous Raman microscopy, stimulated Raman scattering exhibits an orders-of-magnitude faster imaging speed by virtue of optical amplification of the vibrational excitation rate. Photon energy dissipates into vibrational levels during both Raman processes, but with drastically different efficiency. As shown by Eq. (4), the acceleration factor, $r_{stim.\ Raman}/r_{spon.Raman}$, could be estimated for the SRS imaging apparatus reported in Ref. (67). 5mM methanol, which corresponds to about 300,000 C-H vibrational oscillators within the laser focal volume, gives a stimulated Raman loss signal of about $\Delta I_{SRS}/I_p \sim 7\times10^{-8}$. With a known $\sigma_{Raman} \sim 10^{-29}$ cm^2 for one C-H bond, the total spontaneous Raman scattering cross sections of $3*10^5$ C-H vibrational oscillators will add up to be $3*10^{-24}$ cm^2. Given the laser waist area of pump beam being 10^{-9} cm^2 under a tight focus, one would expect to produce a relative spontaneous Raman scattering signal with $\Delta I_{spon.Raman}/I_p = (3*10^{-24}\ \text{cm}^2)/(10^{-9}\ \text{cm}^2) \sim 3*10^{-15}$. Therefore, $r_{stim.Raman}/r_{spon.Raman}$ is estimated to be as high as $7*10^{-8}/3*10^{-15} \sim 10^7$, which accounts for the orders-of-magnitude acceleration of imaging speed so that video-rate SRS microscopy for live animal imaging becomes feasible (71).

Having achieved label-free vibrational specificity, unprecedented imaging speed and superb detection sensitivity, SRS has opened up a wide range of chemical imaging applications in biomedical science and technology by targeting various vibrational bands (see Table 3). As shown in Fig. 5, live cells can be imaged without external labeling by directly targeting different chemical moieties (67-69). Tissue pathologies (72) and food products (73) can be analyzed without applying any dye staining. Reaction kinetics of biopolymer lignin under a chemical treatment can be imaged *in situ* with high spatial and temporal resolution (74). Small molecules such as drugs and metabolites can be monitored and followed inside tissues, as shown in Fig. 6. Lipid storage of *C. elegans* and its genetic regulation can be explored *in vivo* when combined with genetic manipulation of this model organism (75). As illustrated in Fig. 3 (e) and (f), unlike CARS microscopy, SRS only probes the lipid contribution from intestine and hypodermal without the non-resonant background contribution from other tissues, representing a major advantage for high-throughput genetic screening analysis. By implementing a multiplex spectral imaging mode with a spectrally shaped broadband excitation pulse, more specific and detailed spectral features in the congested C-H and O-H region (2800~3100cm^{-1}) can be efficiently picked up even in the presence of interfering species (70).

Another nonlinear dissipation coherent process is two-photon absorption. Historically two-photon absorption was the first nonlinear quantum transition to be explored, having been

predicted in 1931 by Goeppert-Mayer (76). The widely used two-photon excited fluorescence spectroscopy and microscopy (7) are based on the sensitive detection of the subsequent fluorescence emission following two-photon absorption by fluorophores. Two-photon absorption is a nearly simultaneous absorption of two low-energy photons in order to excite a molecule from one state (usually the ground state) to a higher energy electronic state. The sum of the energies of the two photons is resonant with the energy difference between the lower and upper states of the molecule. It fundamentally differs from linear optical absorption in that the strength of absorption depends on the square of the light intensity, and the quantuam mechancal selection rules are different.

Normally two-photon absorption as in two-photon excited fluorescence microscopy (7) is operated under a single beam mode in which molecules are excited by an ultrafast (normally femtosecond or picosecond) pulse train from a mode-locked laser such as a Titanium-Sapphire laser. The two photons involved are drawn from the same laser beam, and thus have similar frequencies within the laser pulse bandwidth. Hence it is difficult to distinguish these two photons spectrally with such a single beam mode.

Two-color dual beam excitation scheme permits two-photon absorption to be compatible with modulation transfer microscopy (77, 78). In principle, two-photon absorption can be equally induced by two photons with different colors, as long as the sum of the energies of the two photons again matches the targeted electronic transition, the two laser pulse trains are temporally synchronized and t overlapped in space. In such a dual-beam mode, blocking the intensity of either color terminates the absorption of the other color by the molecules, as the successful absorption event necessitates the simultaneous presence of the two beams. Two-photon absorption microscopy provides contrast mechanisms for non-fluoresscent chromophores that have appreciable two-photon absorption cross sections (77, 78), as shown in Fig. 7. In the area of biomedicine, examples include beta-carotene, oxy-hemoglobin, deoxy-hemoglobin, melanin and cytochromes.

Dual-beam two photon absorption microscopy and stimulated Raman scattering microscopy are spectroscopically related to each other. They both operate through simutaneous two photon transitions, with one photon drawn from the pump beam and one drawn from the probe beam, respectively, mediated through a virtual state. The difference is that, in the former, the probe photon continues to excite the molecule up to higher energy levels, while in the latter the probe photon brings the molecule down to the vibrational excited state in the ground electronic manifold. In addition, both the response functions of two photon absorption microscopy and stimulated Raman scattering microscopy for a given molcule are given by the imaginary part of third-order nonlinear susceptibility (25). The difference lies in the fact that the former corresponds to two-photon resonance while the latter is assocated with the vibrational resonance.

PUMP-PROBE MICROSCOPY

Pump-probe spectroscopy has been widely used to study the time-dependent ultrafast phenomena. In this section, we will discuss their applications in chemical imaging: stimulated emission microscopy, excited state absorption microscopy, and ground state depletion microscopy.

The theoretical foundation of stimulated emission was first established by Einstein in 1917 (79). The phenomenon was later confirmed experimentally in 1928. An atom or molecule in its excited electronic state can be stimulated down to the ground state by an incident photon with the appropriate frequency, resulting in the creation of a new coherent photon identical to the original incident one in all physical aspects including energy, polarization and phase.

From the perspective of the molecules, excited state population de-excitation occurs simultaneously with the stimulated emission process. Such a population dumping aspect has been utilized in spectroscopy and microscopy, such as in stimulated emission pumping (80), super-resolution fluorescence microscopy (81) and in fluorescence lifetime imaging (82). From the perspective of radiation fields, stimulated emission represents a process of intensity gaining of the incident field. This is precisely the working principle for light amplification in the laser.

The light-amplification aspect of stimulated emission has recently been demonstrated as a contrast mechanism for highly sensitive imaging of non-fluorescent chromophores (83), summarized in Fig. 8. Certain chromophores, such as haemoglobin and cytochromes, absorb light intensely but have undetectable fluorescence in practice. This is so because their spontaneous emission is dominated by their fast non-radiative decay (which can be four orders of magnitude faster than the their rate of spontaneous emission) from the excited state (84). With the introduction of a stimulated emission pulse with appropriate time delay and energy, the chromophore, after being photo-excited to the excited state by a pump pulse, is much more likely to be brought down to the ground state through the radiative decay (which consists of spontaneous emission and stimulated emission) channel compared to through the non-radiative decay. As a result of the new photons radiated by the molecule, the intensity of the stimulation beam is concurrently increased. Although the gain after interacting with the photo-excited chromophores is small, it can be extracted by high-frequency demodulation, making the chromophore detectable.

The pump beam and probe beam have to be in the form of ultra-short (a few hundred femtoseconds) pulse trains to effectively interrogate the transient excited states, as the excited lifetimes of those non-fluorescent chromophores are extremely brief (less than one picosecond). Hence, the need for ultrashort pulses in stimulated emission microscopy is fundamentally different from that in parametric generation microscopy or nonlinear dissipation microscopy. As a result, the pump pulse train and the probe pulse train do not need to overlap in time. In fact, the probe pulse train is delayed (by a few hundred femtoseconds) with respect to the pump pulse train, to permit the molecule enough time to vibrationally relax on the electronic excited state. This delay is also useful to separate the stimulated emission from other instantaneous processes such as stimulated Raman scattering.

Stimulated emission microscopy exhibits a few advantages over direct one-beam absorption microscopy for bio-imaging, although they both probe the electronic spectrum of the chromophore. First, the stimulated emission signal is only generated at the laser spot, offering 3D sectioning. Second, the high frequency modulation transfer scheme provides shot-noise limited detection sensitivity, while one-beam absorption suffers from laser intensity noise at low frequencies. Third, the absorption approach cannot distinguish true optical absorption from light scattering from heterogeneous biological samples, as both effects are manifested as light extinction at the detector. In contrast, stimulated emission microscopy measures the response of the probe beam intensity only at the pump beam modulation frequency, filtering out the probe beam intensity variations due to sample scattering at low frequencies.

Another pump-probe microscopy is based on excited state absorption, as shown in Fig. 9. Compared to two-photon absorption via an intermediate virtual state, excited state absorption can significantly enhance the overall signal by bringing a resonance between a real intermediate electronic state with the pump beam (85-87). For example, *ex vivo* and *in vivo* imaging of blood vessels in mouse ears have been demonstrated with dual beam 775nm and 650nm, by using the charge transfer absorption band of oxy-hemoglobin and deoxy-

hemoglobin in the near IR. Such an excited state absorption imaging modality opens possibilities for oxygenation imaging based on differences in excited-state dynamics between oxy-hemoglobin and deoxy-hemoglobin (87).

Finally modulation transfer microscopy can also be applied to ground state depletion spectroscopy. Unlike stimulated emission, ground state depletion employs pump and probe pulses that are both resonant with the absorption band of the chromophore of the ground state (Fig 10(a)). In the absence of the pump pulse, the probe pulse is getting absorbed and attenuated by the chromophores. But after being excited to the higher electronic state by the pump pulse, the chromophore would then absorb the subsequent probe pulse to a lesser extent, because of the transient depletion of the ground state population. Hence, the presence of the pump beam will result in a relative gain of the probe beam intensity.

The ground state depletion effect can also be created by using continuous-wave laser beams under steady state condition. Very recently, it has been employed to detect an absorption signal from single molecules in condensed phase at room temperature with shot-noise limited sensitivity (88). As shown in Fig. 10, the peak value of ground state depletion signal from a single Atto647N molecule in PMMA film, $\delta\delta P/P \sim 13.5\times10^{-8}$, coincides well with the lateral position of the peak in the simultaneous fluorescence scan. As expected, average of the scanned lines across the photobleached molecule exhibits no signal.

CONCLUDING REMARKS

While fluorescence labeling and imaging have become increasingly sophisticated (89-91), many more molecular species cannot or should not be labeled in biomedicine and material sciences. To this end, coherent nonlinear optical microscopy, especially nonlinear dissipation microscopy and pump-probe microscopy, represents an emerging direction for non-fluorescent optical imaging with high sensitivity and specificity. Exciting applications in various areas are expected for many years to come.

Acknowledgments

We wish to thank many colleagues and collaborators who have contributed to the development and applications of stimulated Raman scattering microscopy, stimulated emission microscopy and ground state depletion microscopy, in particular, B. G. Saar, Shasha Chong, G. R. Holtom, M. Roeffaers, X. Zhang, R. Roy, J. C. Tsai, J. X. Kang, M. C. Wang, S. Y. Ding, and G. Ruvkun. This research was supported by grants from the Department of Energy (DOE)'s Basic Energy Sciences program (DE-FG02-07ER15875), DOE's Office of Biological and Environment Research (DE-FG02-07ER64500), and NSF (grant DBI-0649892 and grant CHE-0634788), NIH Director's Pioneer Award and the Transformative R01 grant, the Bill & Melinda Gates Foundation, and Pfizer Global Medical.

References

1. Lakowicz, JR. Principles of Fluorescence Spectroscopy. Plenum Press; 1983.
2. Pawley, JB., editor. Handbook of Biological Confocal Microscopy. 3rd ed. Springer; 2006.
3. Chalfie M, Tu Y, Euskirchen G, Ward WW, Prasher DC. Green fluorescent protein as a marker for gene expression. Science. 1994; 263:802–805. [PubMed: 8303295]
4. Tsien RY. The green fluorescent protein. Annu. Rev. Biochem. 1998; 67:509–544. [PubMed: 9759496]
5. Zhang J, Campbell RE, Ting AY, Tsien RY. Creating new fluorescent probes for cell biology. Nature Rev. Mol. Biol. 2002; 3:906–918.
6. Michalet X, Pinaud FF, Bentolila LA, Tsay JM, Doose S, Li JJ, Sundaresan G, Wu AM, Gambhir SS, Weiss S. Quantum dots for live cells, in vivo imaging, and diagnostics. Science. 2005; 307:538–544. [PubMed: 15681376]
7. Denk W, Strickler J, Webb WW. Two-photon laser scanning fluorescence microscopy. Science. 1990; 248:73–6. [PubMed: 2321027]

8. Moerner WE, Orrit M. Illuminating single molecules in condensed matter. Science. 1999; 283:1670–76. [PubMed: 10073924]
9. Xie XS, Trautman JK. Optical studies of single molecules at room temperature. Annu. Rev. Phys. Chem. 1998; 49:441–80. [PubMed: 15012434]
10. Hell SW. Far-field optical nanoscopy. Science. 2007; 316:1153–1158. [PubMed: 17525330]
11. Levenson, MD.; Kano, SS. Introduction to nonlinear laser spectroscopy. Academic Press; San Diego: 1988.
12. Hellwarth R, Christensen P. Nonlinear optical microscopic examination of structure in polycrystalline ZnSe. Opt. Comm. 1974; 12:318–322.
13. Sheppard CJR, Kompfner R, Gannaway J, Walsh D. Scanning harmonic optical microscope. IEEE J. Quantum Electron. 1977; 13E:100D.
14. Nuriya M, Jiang J, Nemet B, Eisenthal KB, Yuste R. Imaging membrane potential in dendritic spines. Proc. Natl. Acad. Sci. USA. 2006; 103:786–790. [PubMed: 16407122]
15. Barad Y, Eisenberg H, Horowitz M, Silberberg Y. Nonlinear scanning laser microscopy by third harmonic generation. Appl. Phys. Lett. 1997; 70:922–924.
16. Squier JA, Muller M, Brakenhoff GJ, Wilson KR. Third harmonic generation microscopy. Opt. Express. 1998; 3:315–324. [PubMed: 19384376]
17. Potma EO, Boeij WPD, Wiersma DA. Nonlinear coherent four-wave mixing in optical microscopy. J. Opt. Soc. Am. B. 2000; 17:1678–84.
18. Min W, Lu S, Rueckel M, Holtom GR, Xie XS. Near-degenerate four-wave-mixing microscopy. Nano Lett. 2009; 9:2423–2426. [PubMed: 19432483]
19. Kim H, Sheps T, Collins PG, Potma EO. Nonlinear optical imaging of individual carbon nanotubes with four-wave-mixing microscopy. Nano Lett. 2009; 9:2991–2995. [PubMed: 19637886]
20. Campagnola PJ, Clark HA, Mohler WA, Lewis A, Loew LW. Second-harmonic imaging microscopy for visualizing biomolecular arrays in cells, tissues and organism. Nature Biotech. 2003; 21:1356–1360.
21. Zipfel WR, Williams RM, Christie R, Nikitin AY, Hyman BT, Webb WW. Live tissue intrinsic emission microscopy using multiphoton-excited native fluorescence and second harmonic generation. Proc. Natl. Acad. Sci. USA. 2003; 100:7075–7080. [PubMed: 12756303]
22. Clark, RJH.; Hester, RE., editors. Advances in Nonlinear Spectroscopy. Vol. 15. John Wiley and Sons Ltd.; New York: 1988.
23. Turrell, G.; Corset, J. Raman Microscopy: Developments and Applications. Academic Press; San Diego: 1996.
24. Maker PD, Terhune RW. Study of optical effects due to an induced polarization third order in the electric field strength. Phys. Rev. 1965; 137:A801–18.
25. Boyd, RW. Nonlinear Optics. Academic; London: 2003.
26. Petrov GI, Arora R, Yakovlev VV, Wang X, Sokolov AV, Scully MO. Comparison of coherent and spontaneous Raman microspectroscopies for noninvasive detection of single bacterial endospores. Proc. Natl. Acad. Sci. USA. 2007; 104:7776–7779. [PubMed: 17483468]
27. Pestov D, Ariunbold GO, Wang X, Murawski RK, Sautenkov VA, Sokolov AV, Scully MO. Coherent versus incoherent Raman scattering: molecular coherence excitation and measurement. Opt. Lett. 2007; 32:1725–1727. [PubMed: 17572760]
28. Dogariu A, Goltsov A, Xia H, Scully MO. Concentration dependence in coherent Raman scattering. J. Mod. Opt. 2008; 55:3255–3261.
29. Cheng JX, Xie XS. Coherent anti-Stokes Raman scattering microscopy: Instrumentation, theory, and applications. J. Phys. Chem. B. 2004; 108:827–840.
30. Müller M, Zumbusch A. Coherent anti-Stokes Raman Scattering Microscopy. Chemphyschem. 2007; 8:2156–70. [PubMed: 17768730]
31. Evans CL, Xie XS. Coherent anti-Stokes Raman scattering microscopy: Chemical Imaging for Biology and Medicine. Annu. Rev. Anal. Chem. 2008; 1:883–909.
32. Duncan MD, Reintjes J, Manuccia TJ. Scanning coherent anti-Stokes Raman microscope. Opt. Lett. 1982; 7:350–52. [PubMed: 19714017]

33. Zumbusch A, Holtom GR, Xie XS. Three-dimensional vibrational imaging by coherent anti-Stokes Raman scattering. Phys. Rev. Lett. 1999; 82:4142–4145.
34. Volkmer A, Cheng J, Xie XS. Vibrational imaging with high sensitivity via epi-detected coherent anti-Stokes Raman scattering microscopy. Phys. Rev. Lett. 2001; 87:23901.
35. Evans CL, Potma EO, Puoris'haag M, Cote D, Lin CP, Xie XS. Chemical imaging of tissue in vivo with video-rate coherent anti-Stokes Raman scattering microscopy. Proc. Natl. Acad. Sci. USA. 2005; 102:16807–12. [PubMed: 16263923]
36. Nan X, Cheng JX, Xie XS. Vibrational imaging of lipid droplets in live fibroblast cells with coherent anti-Stokes Raman scattering microscopy. J. Lipid Res. 2003; 44:2202–2208. [PubMed: 12923234]
37. Wang HW, Fu Y, Huff TB, Le TT, Wang H, Cheng JX. Chasing lipids in health and diseases by coherent anti-Stokes Raman scattering microscopy. Vibrat. Spectrosc. 2009; 50:160–167.
38. Begin S, Belanger E, Laffray S, Vallee R, Cote D. In vivo optical monitoring of tissue pathologies and diseases with vibrational contrast. J. Biophoton. 2009; 2:632–642.
39. Enejder A, Brackmann C, Svedberg F. Coherent anti-Stokes Raman scattering microscopyof cellular lipid storage. IEEE J. Sel. Top. Quant. Electron. 2010; 16:506–515.
40. Le TT, Duren HM, Slipchenko MN, Hu CD, Cheng JX. Label-free quantitative analysis of lipid metabolism in living Caenorhabditis elegans. J. Lipid Res. 2010; 51:672–677. [PubMed: 19776402]
41. Cheng JX, Book LD, Xie XS. Polarization coherent anti-Stokes Raman scattering microscopy. Opt. Lett. 2001; 26:1341–43. [PubMed: 18049602]
42. Lu F, Zheng W, Sheppard C, Huang Z. Interferometric polarization coherent anti-Stokes Raman scattering (IP-CARS) microscopy. Opt. Lett. 2008; 33:602–604. [PubMed: 18347723]
43. Volkmer A, Book LD, Xie XS. Time-resolved coherent anti-Stokes Raman scattering microscopy: imaging based on Raman free induction decay. Appl. Phys. Lett. 2002; 80:1505–7.
44. Evans CL, Potma EO, Xie XS. Coherent anti-Stokes Raman scattering interferometry: determination of the real and imaginary components of nonlinear susceptibility $\chi^{(3)}$ for vibrational microscopy. Opt. Lett. 2004; 29:2923–2925. [PubMed: 15645825]
45. Lim SH, Caster AG, Leone SR. Single-pulse phase-control interferometric coherent anti-Stokes Raman scattering spectroscopy. Phys. Rev. A. 2005; 72:41803.
46. Marks DL, Boppart SA. Nonlinear interferometric vibrational imaging. Phys. Rev. Lett. 2004; 92:123905. [PubMed: 15089675]
47. Potma EO, Evans CL, Xie XS. Heterodyne coherent anti-Stokes Raman scattering (CARS) imaging. Opt. Lett. 2006; 31:241–43. [PubMed: 16441043]
48. von Vacano B, Buckup T, Motzkus M. Highly sensitive single-beam heterodyne coherent anti-Stokes Raman scattering. Opt. Lett. 2006; 31:2495–2497. [PubMed: 16880867]
49. Jurna M, Korterik JP, Otto C, Herek JL, Offerhaus HL. Background free CARS imaging by phase sensitive heterodyne CARS. Opt. Express. 2008; 16:15863–15869. [PubMed: 18825222]
50. Dudovich N, Oron D, Silberberg Y. Single-pulse coherently controlled nonlinear Raman spectroscopy and microscopy. Nature. 2002; 418:512–514. [PubMed: 12152073]
51. Lim SH, Caster AG, Nicolet O, Leone SR. Chemical imaging by single pulse interferometric coherent anti-Stokes Raman scattering microscopy. J. Phys. Chem. B. 2006; 110:5196–5204. [PubMed: 16539448]
52. Li H, Ahmasi Harris D, Xu B, Wrzesinski PJ, Lozovoy VV, Dantus M. Coherent mode-selective Raman excitation towards standoff detection. Opt. Express. 2008; 16:5499–5504. [PubMed: 18542653]
53. Silberberg Y. Quantum coherent control for nonlinear spectroscopy and microscopy. Annu. Rev. Phys. Chem. 2009; 60:277–92. [PubMed: 18999997]
54. Vartiainen EM, Rinia HA, Müller M, Bonn M. Direct extraction of Raman line-shapes from congested CARS spectra. Opt. Express. 2006; 14:3622–3630. [PubMed: 19516509]
55. Liu Y, Lee YJ, Cicerone MT. Broadband CARS spectral phase retrieval using a time-domain Kramers-Kronig transform. Opt. Lett. 2009; 34:1363–1365. [PubMed: 19412273]

56. Ganikhanov F, Evans CL, Saar BG, Xie XS. High sensitivity vibrational imaging with frequency modulation coherent anti-Stokes Raman scattering microscopy. Opt. Lett. 2006; 31:1872–74. [PubMed: 16729099]
57. Saar BG, Holtom GR, Freudiger CW, Ackermann C, Hill W, Xie XS. Intracavity wavelength modulation of an optical parametric oscillator for coherent Raman microscopy. Opt. Express. 2009; 17:12532–12539. [PubMed: 19654655]
58. Woodbury EJ, Ng WK. Proc. Inst. Radio Eng. 1962; 50:2347–2348.
59. Jones WJ, Stoicheff BP. Inverse Raman spectra: induced absorption at optical frequencies. Phys. Rev. Lett. 1964; 13:657–659.
60. Bloembergen N. The stimulated Raman effect. Am. J. Phys. 1967; 35:989–1023.
61. Owyoung A. Coherent Raman gain spectroscopy using CW laser sources. IEEE J. Quantum Electron. 1978; QE-14:192–203.
62. Levine BF, Shank CV, Heritage JP. Surface vibrational spectroscopy using stimulated Raman scattering. IEEE J. Quantum Electron. 1979; QE-15:1418–1432.
63. Levenson MD, Moerner WE, Horne DE. FM spectroscopy detection of stimulated Raman gain. Opt. Lett. 1983; 8:108–110. [PubMed: 19714152]
64. Kukura P, McCamant DW, Mathies RA. Femtosecond stimulated Raman spectroscopy. Annu. Rev. Phys. Chem. 2007; 58:461–88. [PubMed: 17105414]
65. Fang C, Frontiera RR, Tran R, Mathies RA. Mapping GFP structure evolution during proton transfer with femtosecond Raman spectroscopy. Nature. 2009; 462:200–204. [PubMed: 19907490]
66. Ploetz E, Laimgruber S, Berner S, Zinth W, Gilch P. Femtosecond stimulated Raman microscopy. Appl. Phys. B. 2007; 87:389–393.
67. Freudiger CW, Min W, Saar BG, Lu S, Holtom GR, He C, Tsai JC, Kang JX, Xie XS. Label-free biomedical imaging with high sensitivity by stimulated Raman scattering microscopy. Science. 2008; 322:1857–1861. [PubMed: 19095943]
68. Nandakumar P, Kovalev A, Volkmer A. Vibrational imaging based on stimulated Raman scattering microscopy. New J. Phys. 2009; 11:033026–35.
69. Ozeki Y, Dake F, Kajiyama S, Fukui K, Itoh K. Analysis and experimental assessment of the sensitivity of stimulated Raman scattering microscopy. Opt. Express. 2009; 17:3651–58. [PubMed: 19259205]
70. Freudiger CW, Min W, Holtom GR, Xu B, Dantus M, Xie XS. 2010 submitted.
71. Saar BG, Freudiger CW, Stanley MC, Holtom GR, Xie XS. 2010 submitted.
72. Freudiger CW, Saar BG, Xie XS, Kesari S, Young GS. 2010 submitted.
73. Roeffaers MBJ, Zhang X, Freudiger CW, Saar BG, van Ruijven M, van Dalen G, Xiao C, Xie XS. 2010 Submitted.
74. Saar BG, Zeng Y, Freudiger CW, Liu YS, Himmel ME, Xie XS, Ding SY. Label-free, real-time monitoring of biomass processing with stimulated Raman scattering microscopy. Angew. Chem. Int. Ed. 2010; 49:5476–5479.
75. Wang MC, Min W, Ruvkun G, Xie XS. 2010 submitted.
76. Goeppert-Mayer M. Über Elementarakte mit zwei Quantensprüngen. Ann. Phys. 1931; 9:273–95.
77. Warren WS, Fischer MC, Ye T. Novel nonlinear contrast improves deep-tissue microscopy. Laser Focus World. 2007; 43:99–103.
78. Ye T, Fu D, Warren WS. Nonlinear absorption microscopy. Photochem. Photobiol. 2009; 85:631–45. [PubMed: 19170931]
79. Einstein A. On the quantum theory of radiation. Phys. Z. 1917; 18:121.
80. Hamilton CE, Kinsey JL, Field RW. Stimulated emission pumping: new methods in spectroscopy and molecular dynamics. Annu. Rev. Phys. Chem. 1986; 37:493–524.
81. Hell SW, Wichmann J. Breaking the diffraction resolution limit by stimulated emission: stimulated-emission-depletion fluorescence microscopy. Opt. Lett. 1994; 19:780–782. [PubMed: 19844443]
82. Dong CY, So PT, French T, Gratton E. Fluorescence lifetime imaging by asynchronous pump-probe microscopy. Biophys. J. 1995; 69:2234–2242. [PubMed: 8599631]

83. Min W, Lu S, Chong S, Roy R, Holtom GR, Xie XS. Imaging chromophores with undetectable fluorescence by stimulated emission microscopy. Nature. 2009; 461:1105–1109. [PubMed: 19847261]
84. Turro, NJ. Modern Molecular Photochemistry. University Science Books; 1991.
85. Fu D, Ye T, Matthews TE, Chen BJ, Yurtserver G, Warren WS. High-resolution in vivo imaging of blood vessels without labeling. Opt. Lett. 2007; 32:2641–2643. [PubMed: 17873920]
86. Fu D, Ye T, Matthews TE, Yurtsever G, Warren WS. Two-color, two-photon, and excited-state absorption microscopy. J. Biomed. Opt. 2007; 12:054004. [PubMed: 17994892]
87. Fu D, Matthews TE, Ye T, Piletic IR, Warren WS. Label-free in vivo optical imaging of microvasculature and oxygenation Level. J. Biomed. Opt. 2008; 13:040503. [PubMed: 19021307]
88. Chong S, Min W, Xie XS. Ground state depletion microscopy: Room temperature detection of single molecule optical absorption. 2010 submitted.
89. Miller LW, Cornish VW. Selective chemical labeling of proteins in living cells. Curr. Opin. Chem. Biol. 2005; 9:56–61. [PubMed: 15701454]
90. Lin MZ, Wang L. Selective labeling of proteins with chemical probes in living cells. Physiology. 2008; 23:131–141. [PubMed: 18556466]
91. Fernandez-Suarez M, Ting AY. Fluorescent probes for super-resolution imaging in living cells. Nat. Rev. Mol. Cell. Biol. 2008; 9:929–943. [PubMed: 19002208]

FUTURE ISSUES

1. What is the ultimate sensitivity of stimulated Raman scattering microscopy? Can special laser excitation sources significantly enhance the coherence amplitude ρ_{vib}?
2. Can principles (such as entangled photons or squeezed light) and techniques in quantum optics could be borrowed to surmount the shot-noise limited detection sensitivity?
3. Can modulation of other optical properties (such as the frequency, polarization and phase) of the pump beam bring advantages over intensity modulation?
4. How to achieve super-resolution (beyond the diffraction-limited resultion) imaging for coherent nonlinear optical microscopy?
5. Can fiber delivery and fiber-based laser sources reduce the cost and complexity of microscopy systems?

SUMMARY POINTS

1. Non-fluorescent molecules can be imaged in 3D with high sensitivity and specificity by nonlinear dissipation microscopy and pump-probe microscopy through a modulation transfer scheme.
2. High frequency modulation, together with the associated phase-sensitive lock-in detection, removes all the low-frequency laser intensity noise and permits shot-noise limited sensitivity. For biological samples, this avoids the contribution from linear scattering due to heterogeneous refractive index. The ultimate single-molecule sensitivity has already been achieved in a ground state depletion experiment.
3. Compared to the class of parametric generation microscopy, nonlinear dissipation microscopy and pump-probe microscopy exhibit much improved molecular specificity, by directly interrogating real electronic or vibrational transitions instead of the intermediate virtual states.
4. The stimulated coherent excitation of vibrational oscillators by the joint action of pump and Stokes (probe) photons gives rise to a much more efficient vibrational excitation than that of spontaneous Raman microscopy, resulting in orders-of-magnitude improvement in acquisition speed.
5. SRS microscopy overcomes the long-standing difficult of non-resonant background in CARS microscopy, by detecting the direct energy transfer from the laser fields to the vibrational states instead of reading out the vibrational coherence. With the removal of such a background, SRS display a variety of advantages over CARS microscopy, notably, the clean and undistorted spectrum, the shot-noise-limited sensitivity, the strict linear concentration dependence, and the existence of a well-defined point spread function.
6. Two-photon absorption and excited-state absorption microscopy take advantage of the large two-photon absorption cross section of many biomolecules for tissue imaging.
7. Stimulated emission microscopy is capable of image non-fluorescent chromophores with superb sensitivity by virtue of optical amplification of molecular radiation.

(Optical) shot noise: intrinsic statistical uncertainty of the measured light intensity due to the stochastic arrivial of light particles, i.e. photons.

Virtual state: a short-lived intermediate quantum state that mediates otherwise forbidden transitions in a multi-step process.

$\chi^{(3)}$: third-order polarizability which describes the nonlinear tendency of the charge distribution of a molecule to be distorted by an external strong electric field.

$\rho_{vib.}$: off-diagonal element of the density matrix characterizing the coherence between the ground vibrational state and the first excited vibrational state, and the degree to which the molecules in the ensemble oscillate in unison.

Non-resonant CARS background: a four-wave-mixing parametric process generated by the nonlinear electronic response of the sample mediated through virtual states.

k vector: a vector with it s magnitude inversely proportional to the wavelength and its direction paralel to the direction of wave propogation.

Lock-in amplifier: a type of amplifier that can extract a small signal with a known carrier wave from an extremely noisy environment

Chromoproteins: proteins that contains non-fluorescent pigments and hence are capable of absorbing light.

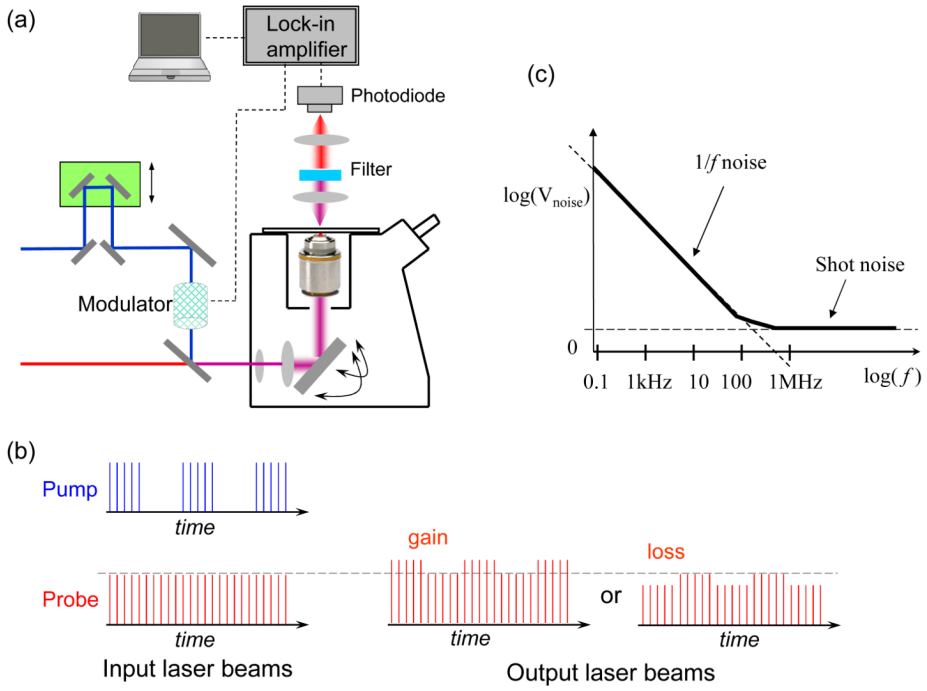

Figure 1.

Principle of nonlinear dissipation microscopy and pump-probe microscopy in which a high-frequency modulation transfer scheme is utilized. (a) The generic experimental scheme. Both pump and probe beams are focused onto a common focal spot with a microscope objective. The intensity (or frequency, polarization, phase, etc) of the pump beam is modulated at a high frequency (>1 MHz), and probe beam after interacting with the sample is collected and detected by a photodiode and then demodulated by a lock-in amplifier. (b) Temporal modulation behaviors of the input and output pump and probe pulse trains before and after interacting with the samples. The probe beam could undergo either a gain or a loss in its intensity. (c) Noise spectrum (log-log plot) of a typical laser source as a function of frequency *f*. In the low frequency range (from DC to kHz), the noise follows the so-called 1/*f* noise. In the higher frequency, the noise approaches the flat floor of shot noise.

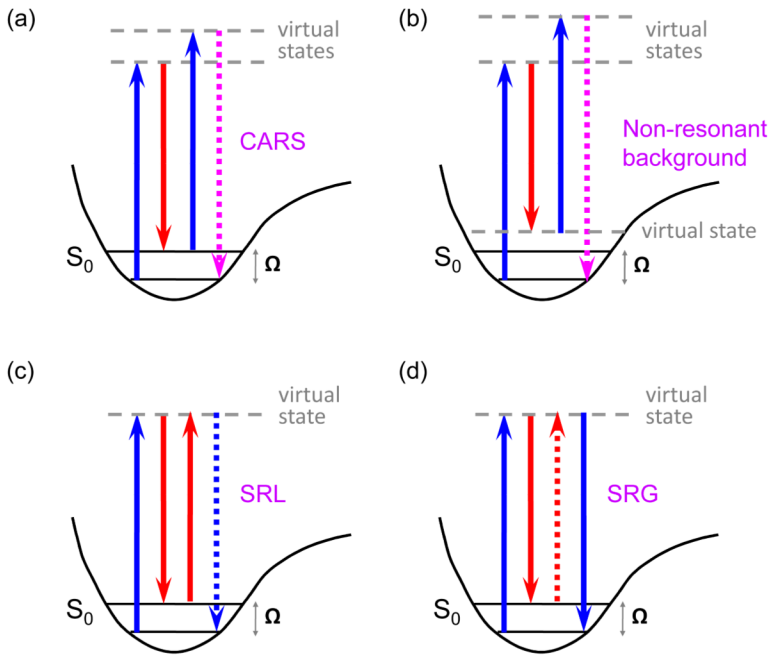

Figure 2.

Energy level diagrams of different third order nonlinear induced polarizations. (a) When the energy difference between pump and probe beam is resonant with a vibrational transition of the molecule, a strong resonant CARS signal at the anti-Stokes frequency is emitted. (b) When the energy difference between pump and probe beam is not resonant with any vibrational transitions of the material, a weak but non-vanishing signal, known as the non-resonant background, is still generated at the anti-Stokes frequency. (c) Stimulated Raman loss (SRL) occurring at the pump field frequency has the opposite (180 degree lag) phase compared to the pump field. (d) Stimulated Raman gain (SRG) occurring at the probe field frequency has the same (zero degree lag) phase with that of the probe field.

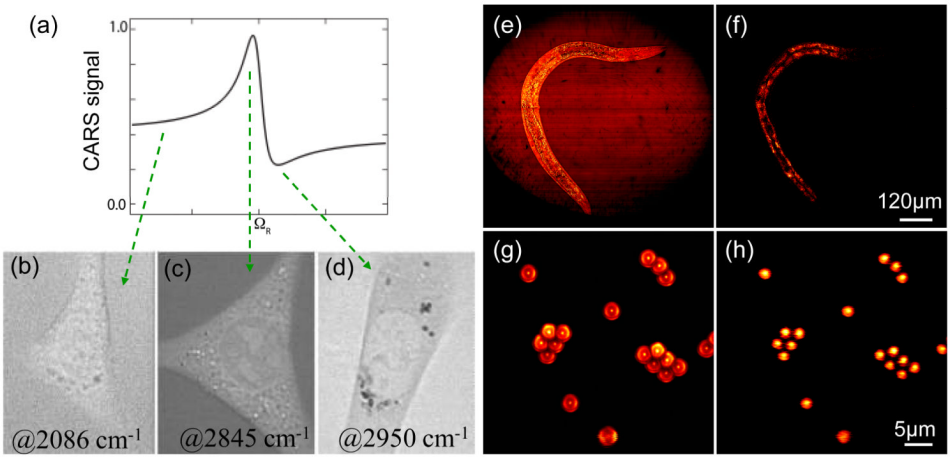

Figure 3.

Comparison between CARS and SRS imaging. (a) The theoretical CARS spectrum resulted from interference between non-resonant background and real part of vibrational resonant contribution. (b)-(d) are forward CARS images of 3T3-L1 cells tuned across the C-H resonance. (b) cell imaged at C-H off resonant condition (2086 cm^{-1}); (c) cell imaged at C-H resonant condition (2845 cm^{-1}); (d) cell imaged at the blue dip of the C-H band at 2950 cm^{-1}. Resonant features appear dark against the non-resonant background; (b)-(d) adapted from Reference (31). Simultaneous (e) epi-CARS and (f) SRS images of a live worm, *C. elegans*, with the Raman shift being set to the lipid band 2845 cm^{-1}. While SRS specifically probes the lipid contribution, CARS contrast is evidently complicated by non-resonant background from non-lipid structures. Simultaneous (g) epi-CARS and (h) SRS images of a layer of 2 μm polystyrene beads spin-coated on a glass coverslip, with Raman shift being at 2845 cm^{-1}. While SRS shows well-behaved round disks for single beads, the corresponding CARS images show a bright ring due to the interference effect occurring at the edge and a bright spot at the center due to the forward going CARS signal being reflected back by the bead/air interface.

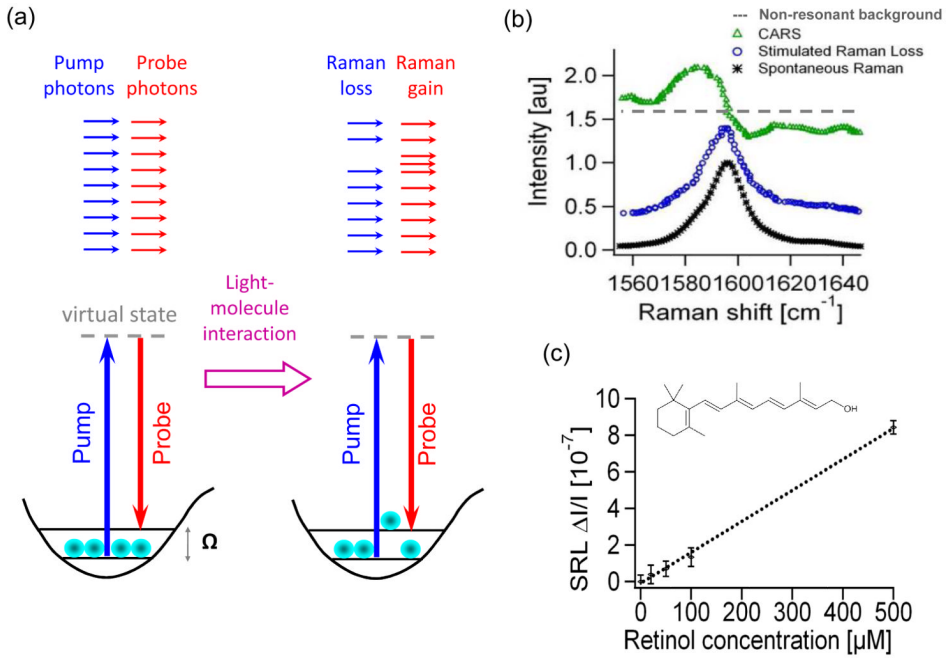

Figure 4.

Principle of stimulated Raman scattering microscopy. (a) Energy diagram of stimulated Raman scattering when the energy difference between pump and probe is resonant with a vibrational transition. Stimulated Raman gain of the probe beam and stimulated Raman loss of the pump beam after interacting with the vibrational oscillators are depicted too. (b) Recorded spectra of the 1595 cm^{-1} Raman peak of 10 mM retinol in ethanol by spontaneous Raman, CARS and SRS. While the distorted CARS spectrum exhibits a typical peak shift, dispersive shape and nonresonant background, SRS spectrum is identical to that of spontaneous Raman. (c) Linear dependence of SRS signal on concentrations of retinol in ethanol at 1595 cm^{-1}. Modulation depth $\Delta I_p/I_p < 10^{-7}$ can be detected. The detection limit was determined to be 50 μM.

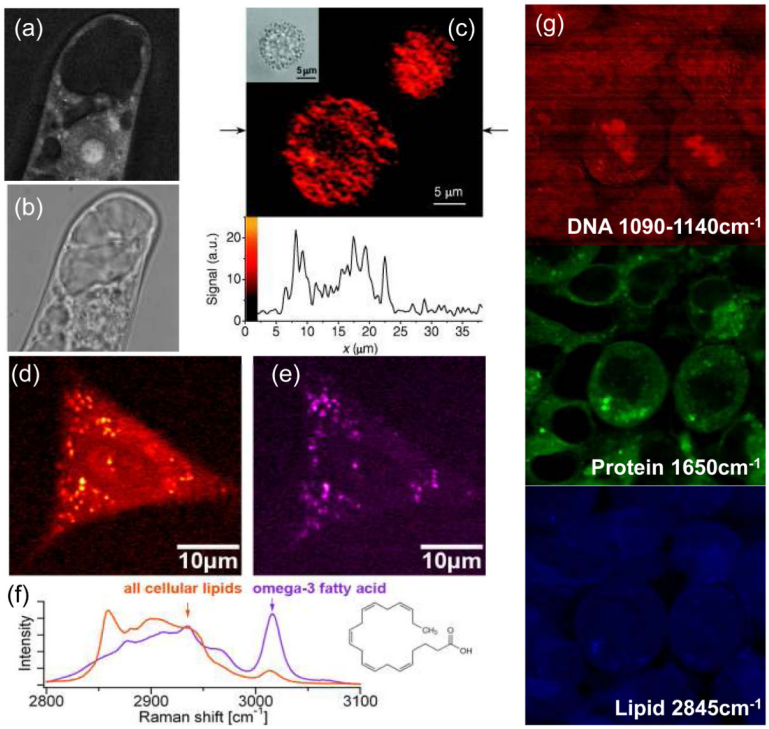

Figure 5.

SRS imaging of live cells at various spectral regions. (a) SRS image and (b) optical transmission microscope image of an unstained tobacco BY2 cultured cell with the Raman shift being set to 2967 cm^{-1}. The nucleus and cell walls of a tobacco BY2 cultured cell are clearly visualized. Figure adapted from Reference (69). (c) SRS image of unstained human HL60 cells in an aqueous environment with the corresponding Raman shift being 1659 cm^{-1} on resonance with the C=C stretching vibrations. Figure adapted from Reference (68). (d) and (e) SRS images of a human lung cancer cell incubated with omega-3 fatty acids at 2920 cm^{-1} and 3015 cm^{-1}, respectively. A clear distinction of saturated and unsaturated lipid distributions is evident. (e) Spontaneous Raman spectrum of oleic acid (with single double C=C bond) and docosahexaenoic acid (with six double C=C bond). The strong peak at 3015cm-1 is characteristic of unsaturated fatty acids. Figures (d)-(f) adapted from Reference (67). (g) Human embryonic kidney cells in metaphase, imaged at three different Raman shifts corresponding to DNA (1090~1140 cm^{-1}), protein (1650 cm^{-1}) and lipids (2845 cm^{-1}), respectively.

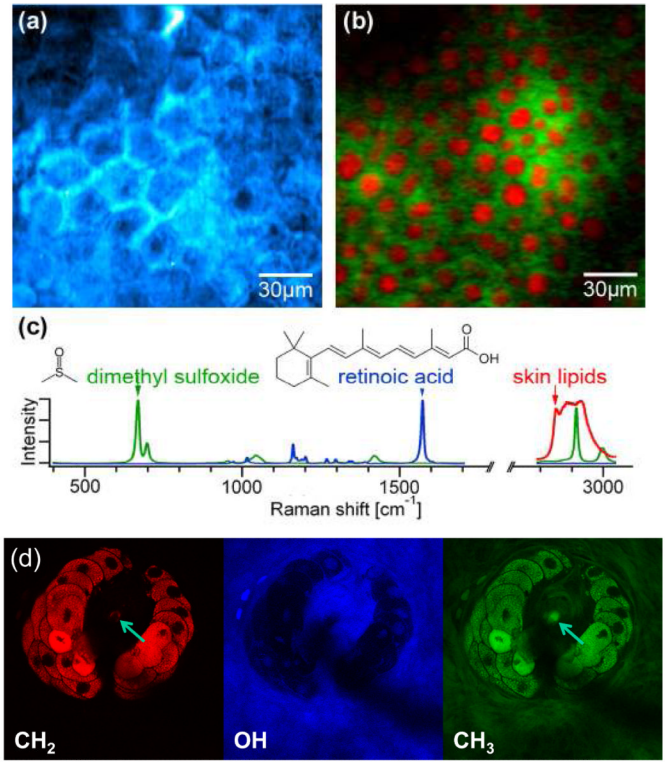

Figure 6.

Tissue imaging by SRS microscopy. Distributions of (a) topically applied compound retinoic acid and (b) penetration enhancer dimethyl sulfoxide (DMSO) in a mouse ear skin. These images were acquired when tuned into the Raman shifts (c) of retinoic acid at 1570 cm^{-1} (blue) and DMSO at 670 cm^{-1} (green). Skin structures are also highlighted by tuning into the CH_2 stretching vibration at 2845 cm^{-1} (red). Adapted from Reference (67). (d) A sebaceous gland embedded in a mouse ear imaged at three different Raman shifts corresponding to lipid CH_2, water OH and protein CH_3. The arrows indicate a hair whose keratin is seen the CH_3 image and oil coating in the CH_2 image. The subcellular resolution reveals the water-containing and lipid-deprived nuclei with reverse contrast.

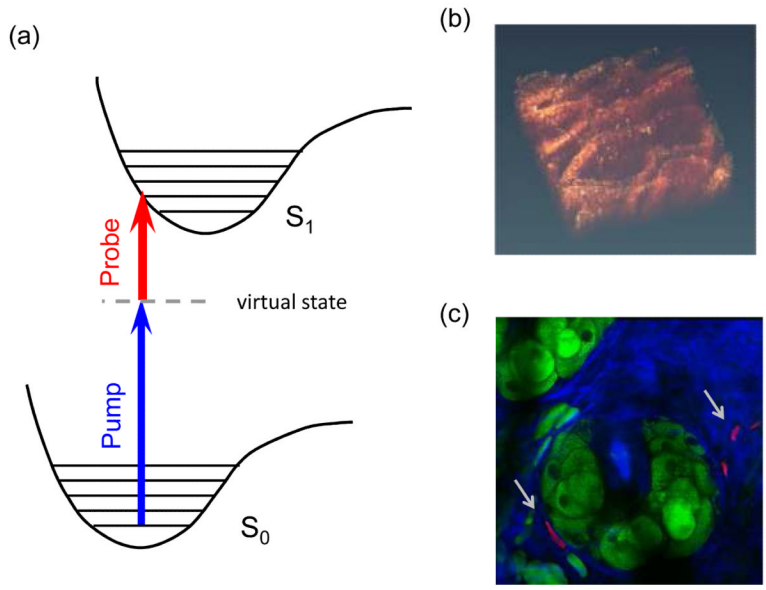

Figure 7.
Two-photon absorption microscopy. (a) Energy diagram of simultaneous two-photon absorption by a high-lying electronic state through an intermediate virtual state. (b) 3D volume rendering of two-photon absorption signal from human melanoma lesions obtained with femtosecond pulse trains of two different colors. Image adapted from Reference (78). (c) Two photon absorption image of microcapillaries in a sebaceous gland of mouse skin with contrast due to hemoglobin in red blood cells (red). Overlaid are lipid (green) and protein (blue) SRS images, taken with the same picosecond pulse trains, at corresponding Raman shifts, showing lipid-rich gland cells and adipocytes as well as protein-rich structures such as hairs and collagen, respectively.

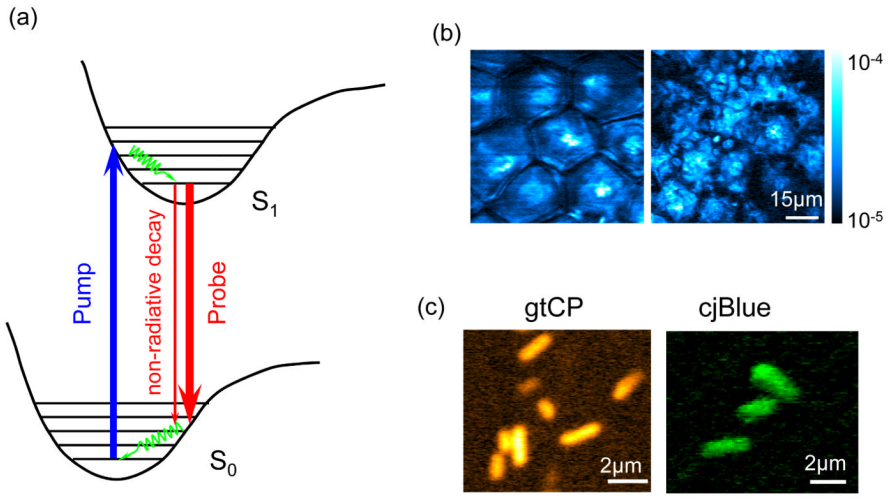

Figure 8.

Stimulated emission microscopy. (a) Energy diagram of stimulated emission. (b) A pair of SEM images of toluidine blue O, a drug used as photosensitizer in photodynamic therapy, at two different z-depths (3 and 25 μm, respectively), delivered onto a mouse ear. Optical sectioning is evident. (c) SEM images of genetically encoded non-fluorescent chromoproteins, gtCP and cjBlue, respectively, inside *E. coli* cells that contain corresponding expression plasmids. Images adapted from Reference (83).

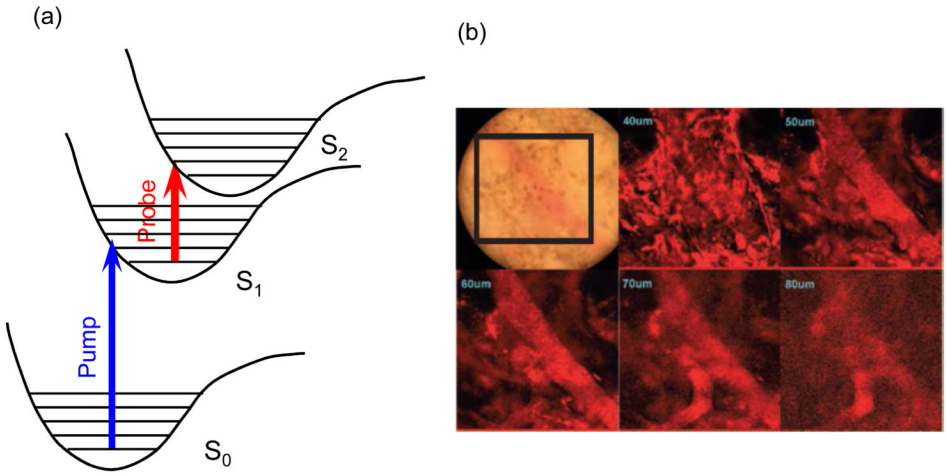

Figure 9.
Excited state absorption microscopy. (a) Energy diagram of sequential two-photon absorption via an intermediate electronic energy state. (b) Bright field image and a series of laser scanning two-color excited-state absorption images from blood at various depths in a mouse ear. Figure adapted from Reference (85).

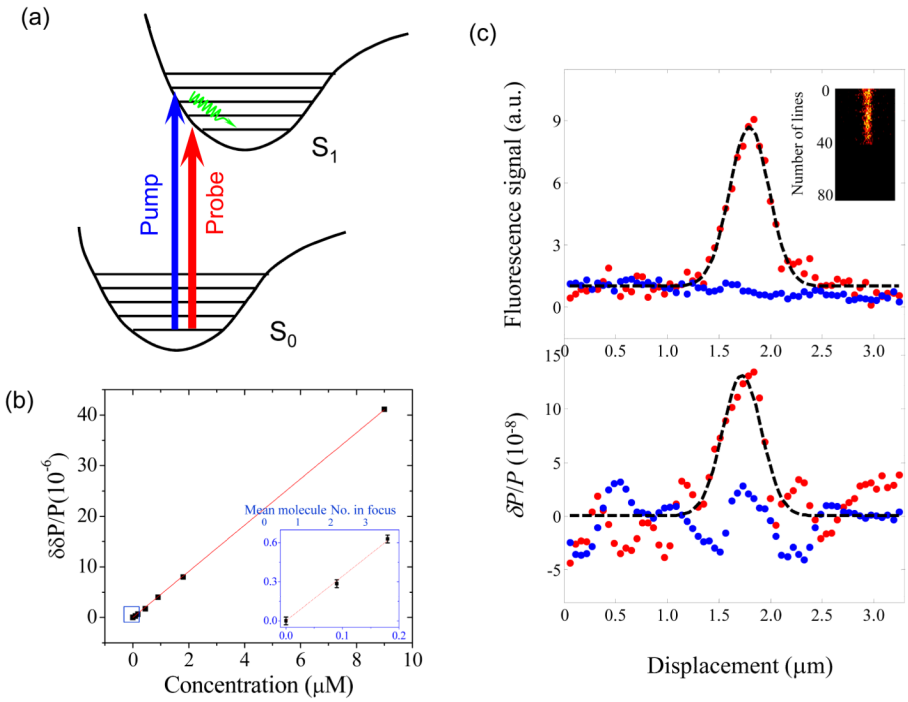

Figure 10.

Ground state depletion micro-spectroscopy of single molecules. (a) Energy diagram of ground state depletion. (b) Ground state depletion signal as a function of concentration of aqueous Atto647N solution. The blue inset indicates the data points at lowest concentrations, with estimated mean molecule numbers in the probe volume. Error bars are for 1s integration time, indicating that single-molecule sensitivity is reachable. (c) Simultaneous fluorescence and ground state depletion line scans for a single Atto647N molecule embedded in PMMA film, averaged before (red) and after (blue) photobleaching. The inset shows the one-dimensional fluorescence image constructed from repeated line scans across the molecule, which underwent abrupt single step photobleaching after 45 lines. Figure adapted from Reference (88).

Table 1

Summary of physical properties of nonlinear dissipation microscopy and pump-probe microscopy and their desirable consequences in bio-imaging.

Properties	Consequences
No need for fluorescence	Imaging non-fluorescent molecules
Targeting electronic or vibrational states	Specificity given by molecular spectrum
High frequency modulation/demodulation	Superb shot-noise limited sensitivity
Overall nonlinear intensity dependence	Intrinsic 3D optical sectioning
Linear concentration dependence	Convenient quantification
Targeted to a high-frequency component	Immune to heterogeneous sample scattering

Table 2

Comparison of spectroscopy and microsocpy aspects between CARS and SRS imaging.

Coherent Anti-Stokes Raman Scattering	Stimulated Raman Scattering
Parametric generation process	Energy transfer process
Existence of non-resonant background	Absence of non-resonant background
Distorted complex spectrum	Identical spectrum to Raman scattering
Limited by laser intensity noise	Shot-noise limited sensitivity
Linear to quadratic concentration dependence	Linear concentration dependence
Complication by spatial coherence	Absence of spatial coherence
Non-existence of point spread function	Existence of point spread function
Contamination by two-photon fluorescence	Immune to background fluorescence

Table 3

Vibrational bands and corresponding Raman shifts used in SRS microscopy

Vibrational modes	Raman shifts	Chemicals	References
O—H stretching	~3250 cm^{-1}	Water	72, 73
(C=)C—H stretching	~3015 cm^{-1}	Unsaturated lipids	67
C—H_3 stretching	~2950 cm^{-1}	Proteins	67, 69
C—H_2 stretching	~2845 cm^{-1}	Saturated lipids	67
N-C=O stretching	~1656 cm^{-}	proteins	68
aryl ring stretching	~1600 cm^{-1}	Lignin	74
conjugated C=C stretching	~1590 cm^{-1}	Retinoic acid	67
asymmetric COC stretching	~1100 cm^{-1}	Cellulose	74
O—P—O symmetric stretching	~1095 cm^{-1}	Nucleic acid	73
Ring breathing of phenylalanine	~1004 cm^{-1}	Proteins	73
S=O stretching	~670 cm^{-1}	DMSO	67